Deciphering and quantifying linear light upconversion in molecular erbium complexes.

Bahman Golesorkhi, Alexandre Fürstenberg, Homayoun Nozary and Claude Piguet*

Supporting Information

(19 pages)

Appendix 1: Experimental Section

The preparation of complexes $[Er(\mathbf{L}\boldsymbol{k})_3](ClO_4)_3$ (**L*k*** = **L1**-**L4**) as well as their exhaustive structural characterization in the solid-state and in solution were reported previously.[32]

Solid-state luminescence data were collected on samples mounted directly onto copper plates using conductive silver glue. Solution experiments were performed using either sealed quartz capillary stuck onto copper plates using conductive silver glue or quartz cells of 5-10 mm path length. Emission spectra were measured on a Horiba Scientific Fluorolog 3 spectrofluorimeter equipped with a visible photomultiplier tube (PMT) (220-850 nm, R928P or 185-1010 nm, R2658P; Hamamatsu). The infrared luminescence spectra were recorded using a NIR solid-state InGaAs detector cooled to 77 K (900-1700 nm, H10330B-75; Hamamatsu).. The low-temperature emission spectra were recorded using an optical closed-cycle cryostat capable of reaching low temperatures down to 5 K in a helium atmosphere (Sumitono HC-4E/Janis Research CCS-900/204N). The emission spectra were corrected for the wavelength-dependent detection sensitivity. Resonant excitations into the $Er(^4I_{9/2}\leftarrow{}^4I_{15/2})$ and $Er(^4I_{11/2}\leftarrow{}^4I_{15/2})$ transitions in $[Er(\mathbf{L}\boldsymbol{k})_3](ClO_4)_3$ (**L*k*** = **L1**-**L4**) were achieved with diode lasers at 801 nm (MDL-H-800-2.5W) and 966 nm (MDL-F-980-10W), respectively, from Changchun New Industries Optoelectronics Technology Co., Ltd (CNI). A 550/88 bandpass filter (Semrock) was placed directly after the sample for visible emission measurements in order to remove the second-order Rayleigh scattering of the laser line. Excitation into the ligand-centered $\pi_1^*\leftarrow\pi$ transition was performed with a diode laser at λ_{exc} = 401 nm (BrixX® 405-1200 HP) manufactured by Omicron-Laserage. The different excitation beams were loosely focused onto the sample with a 30 cm lens to reach an excitation spot size of ≈1.5 mm in diameter (Surface ≈ 0.05 cm^2 or 0.07 cm^2). The mathematical analyses were performed by using Igor Pro® (WaveMetrics Inc.), Origin 2017 (originLab Corporation) and Excel® (Microsoft) softwares. The quantum yields were determined through the relative method[S1] using indocyanine green as reference (ICG, λ_{exc} = 801 nm, Φ_r = 0.132 in ethanol at 298 K, $n_{CH_3CN} = 1.344$, $n_{C_2H_5OH} = 1.361$).[S2] Electronic absorption spectra in the Vis and NIR regions were recorded at 298 K from acetonitrile (ethanol for ICG) solutions with a Perkin-Elmer Lambda 1050 absorption spectrometer using quartz cell of 10 mm path length. Solution emission spectra were recorded in non-deuterated acetonitrile (non-deuterated ethanol for ICG) using quartz cells of 5 mm path length. The emission spectrum of ICG was recorded upon excitation at λ_{exc} = 705 nm using the standard xenon lamp of the Horiba Scientific Fluorolog 3 spectrofluorimeter.

S1 J.-C. G. Bünzli and S. V. Eliseeva, S. V. in *Lanthanide Luminescence: Photophysical, Analytical and Biological Aspects*, Eds P. Hänninen, and H. Härmä, Springer, Berlin Heidelberg, 2011, pp. 1-45.

S2 K. Rurack and M. Spieles, *Anal. Chem.*, 2011, **83**, 1232-1242.

Table S1. Molar absorption coefficients for the mononuclear erbium complexes $[Er(\mathbf{L}\boldsymbol{k})_3]^{3+}$ (**L*k*** = **L1-L4**) and $[Er(\mathbf{L}\boldsymbol{k})_2]^{3+}$ (**L*k*** = **L1**, **L4**) in acetonitrile solution at 298 K and λ_{abs} = 801 nm ($Er(^4I_{9/2}\leftarrow{}^4I_{15/2})$) and λ_{abs} = 966 nm ($Er(^4I_{11/2}\leftarrow{}^4I_{15/2})$).

Compound	ε_{966} / $M^{-1}\cdot cm^{-1}$	ε_{801} / $M^{-1}\cdot cm^{-1}$
$[Er(\mathbf{L1})_2(O_3SCF_3)_2](CF_3SO_3)$	0.80	0.25
$[Er(\mathbf{L4})_2(O_3SCF_3)_2](CF_3SO_3)$	0.64	0.20
$[Er(\mathbf{L1})_3](ClO_4)_3$	0.56	0.24
$[Er(\mathbf{L2})_3](ClO_4)_3$	0.54	0.20
$[Er(\mathbf{L3})_3](ClO_4)_3$	0.54	0.22
$[Er(\mathbf{L4})_3](ClO_4)_3$	0.66	0.20

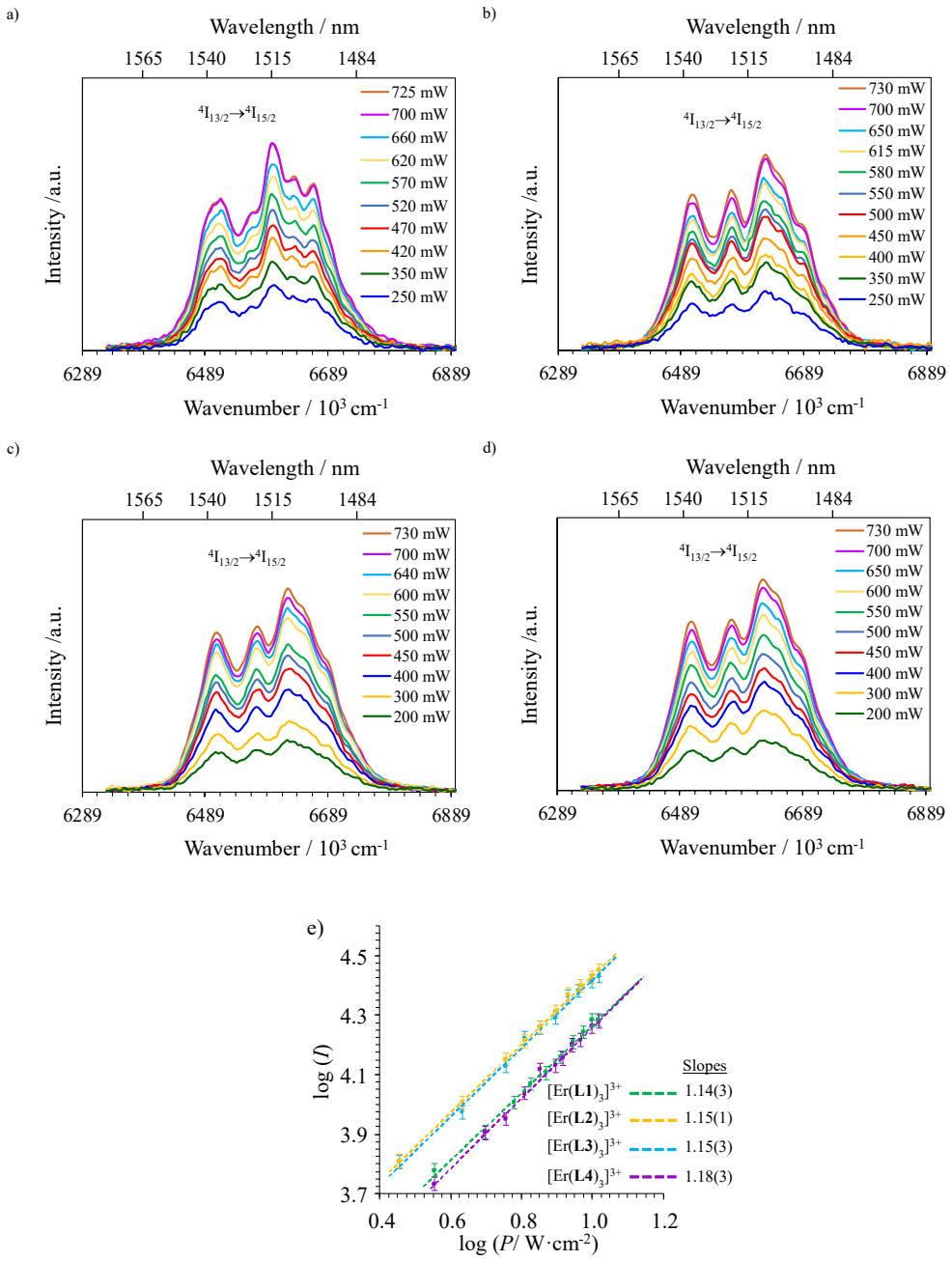

Figure S1. Near-infrared downshifted Er($^4I_{13/2}\rightarrow{}^4I_{15/2}$) emission observed for a) [Er(**L1**)$_3$](ClO$_4$)$_3$, b) [Er(**L4**)$_3$](ClO$_4$)$_3$, c) [Er(**L3**)$_3$](ClO$_4$)$_3$ and d) [Er(**L2**)$_3$](ClO$_4$)$_3$ in acetonitrile solution (10 mM, 298 K) upon laser excitation of the Er($^4I_{9/2}\leftarrow{}^4I_{15/2}$) transition at λ_{exc} = 801 nm ($\tilde{\nu}_{exc}$ = 12284 cm^{-1}) and for different incident pump intensities focused on a spot size of ≈ 0.07 cm^2 and e) corresponding log-log plots of downshifted intensities I as a function of incident pump intensities P (in W·cm^{-2}). The straight lines correspond to extrapolated linear fits.

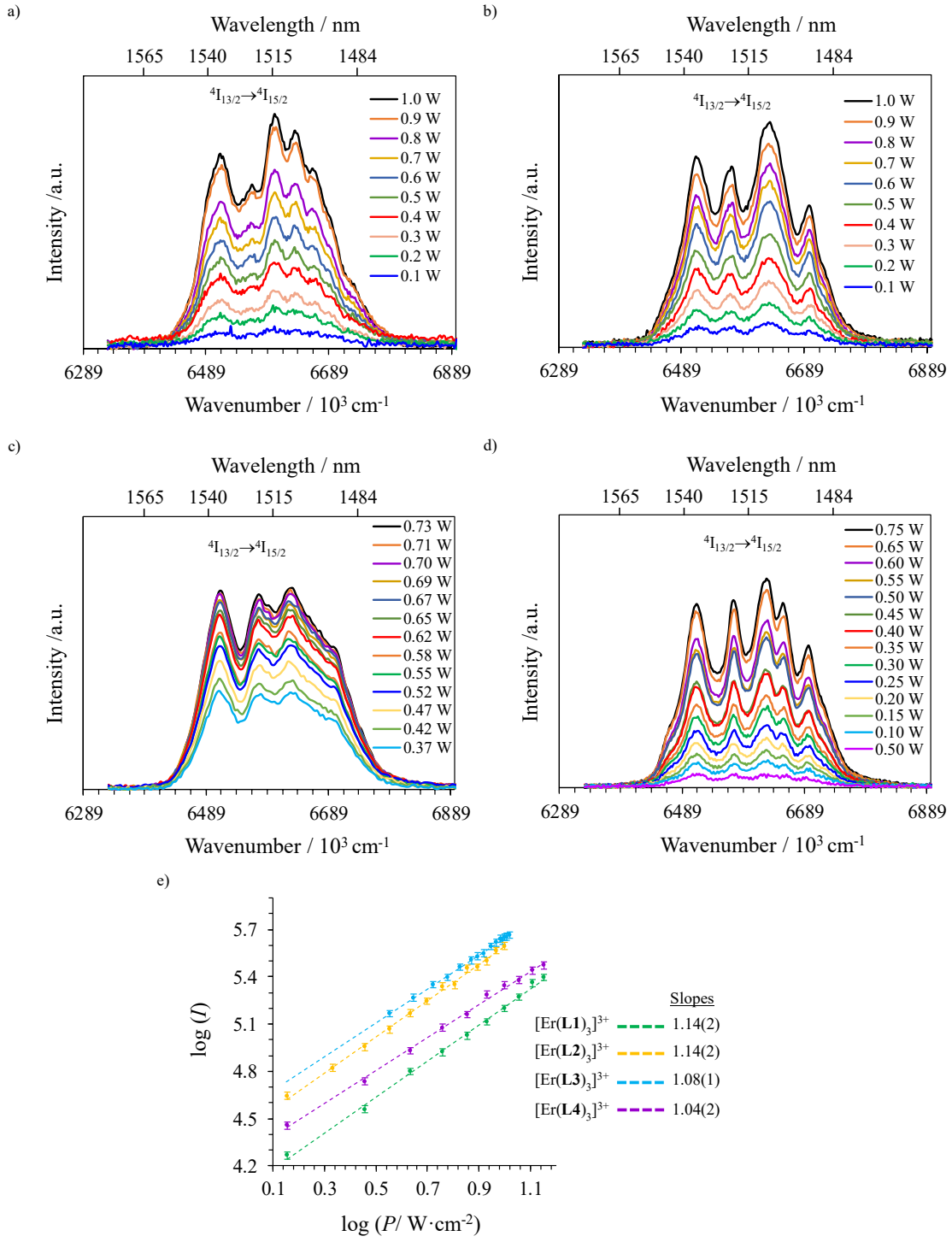

Figure S2. Near-infrared downshifted Er($^4I_{13/2}\rightarrow{}^4I_{15/2}$) emission observed for a) [Er(**L1**)$_3$](ClO$_4$)$_3$, b) [Er(**L4**)$_3$](ClO$_4$)$_3$, c) [Er(**L3**)$_3$](ClO$_4$)$_3$ and d) [Er(**L2**)$_3$](ClO$_4$)$_3$ in the solid state (298 K) upon laser excitation of the Er($^4I_{9/2}\leftarrow{}^4I_{15/2}$) transition at λ_{exc} = 801 nm ($\tilde{\nu}_{exc}$ = 12284 cm^{-1}) and for different incident pump intensities focused on a spot size of ≈ 0.07 cm^2 and e) corresponding log-log plots of downshifted intensities I as a function of incident pump intensities P (in W·cm^{-2}). The straight lines correspond to extrapolated linear fits.

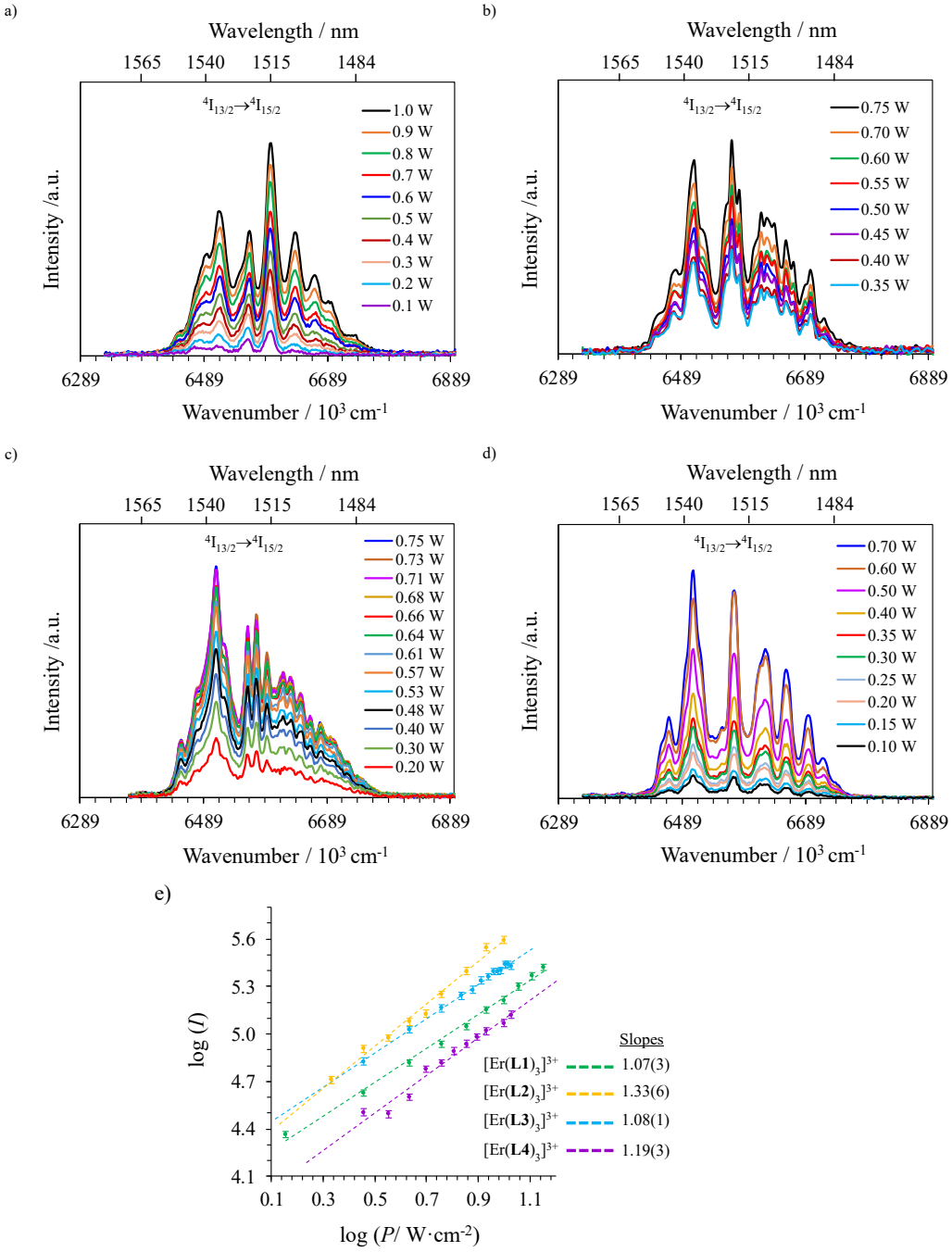

Figure S3. Near-infrared downshifted Er($^4I_{13/2}\rightarrow{}^4I_{15/2}$) emission observed for a) [Er(**L1**)$_3$](ClO$_4$)$_3$ at 20 K, b) [Er(**L4**)$_3$](ClO$_4$)$_3$ at 102 K, c) [Er(**L3**)$_3$](ClO$_4$)$_3$ at 122 K and d) [Er(**L2**)$_3$](ClO$_4$)$_3$ at 116 K in the solid state upon laser excitation of the Er($^4I_{9/2}\leftarrow{}^4I_{15/2}$) transition at λ_{exc} = 801 nm ($\tilde{\nu}_{exc}$ = 12284 cm^{-1}) and for different incident pump intensities focused on a spot size of ≈ 0.07 cm^2 and e) corresponding log-log plots of downshifted intensities I as a function of incident pump intensities P (in W·cm^{-2}). The straight lines correspond to extrapolated linear fits.

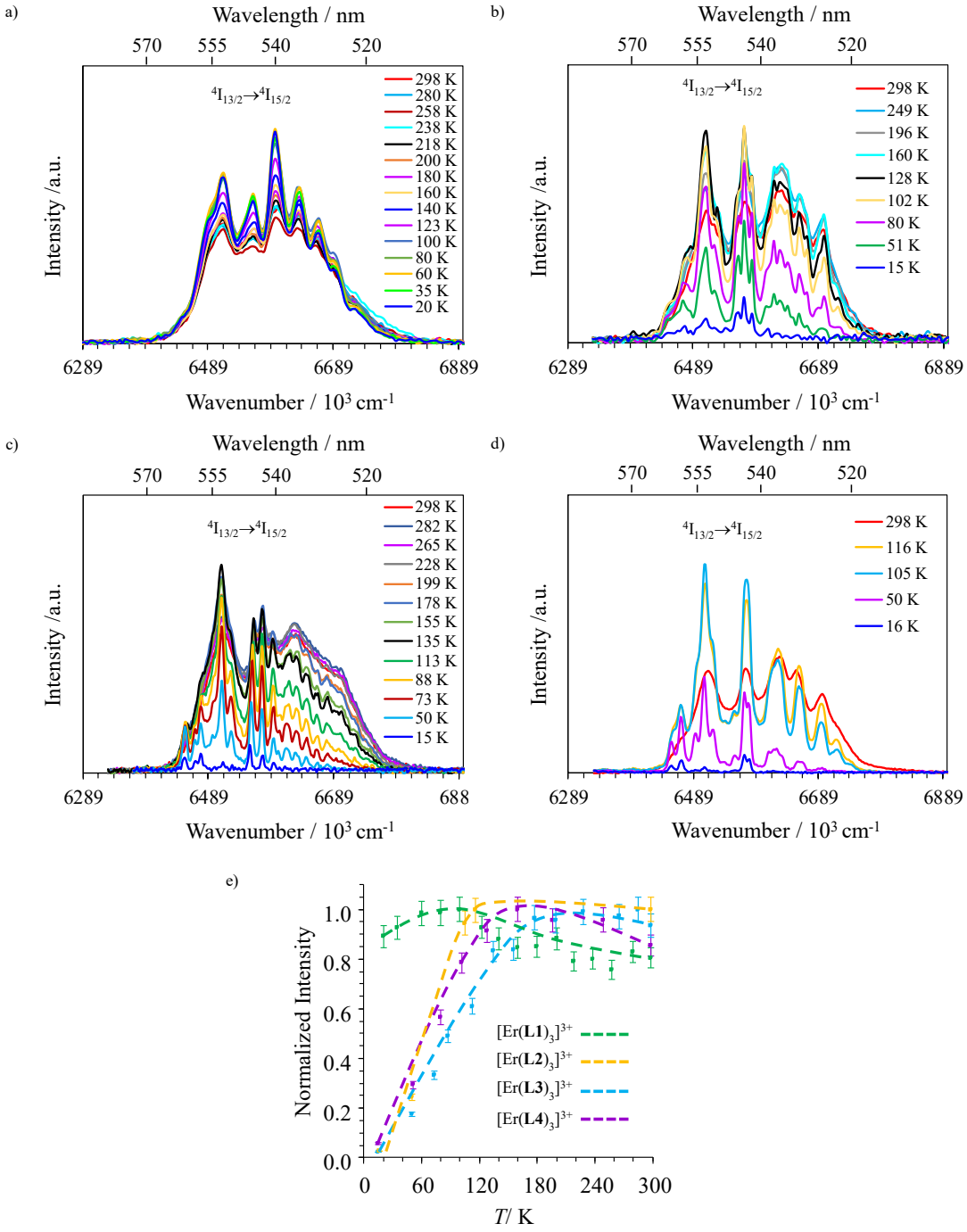

Figure S4. Near-infrared downshifted Er($^4I_{13/2}\rightarrow{}^4I_{15/2}$) emission observed for a) [Er(**L1**)$_3$](ClO$_4$)$_3$, b) [Er(**L4**)$_3$](ClO$_4$)$_3$, c) [Er(**L3**)$_3$](ClO$_4$)$_3$ and d) [Er(**L2**)$_3$](ClO$_4$)$_3$ in the solid state (P = 10 W·cm^{-2} focused on a spot size of ≈ 0.07 cm^2) upon laser excitation of the Er($^4I_{9/2}\leftarrow{}^4I_{15/2}$) transition at λ_{exc} = 801 nm ($\tilde{\nu}_{exc}$ = 12284 cm^{-1}) and for different temperatures and d) associated dependences of the Er-centered near-infrared downshifted emission intensity as a function of temperature. The dashed lines are only guides for the eyes.

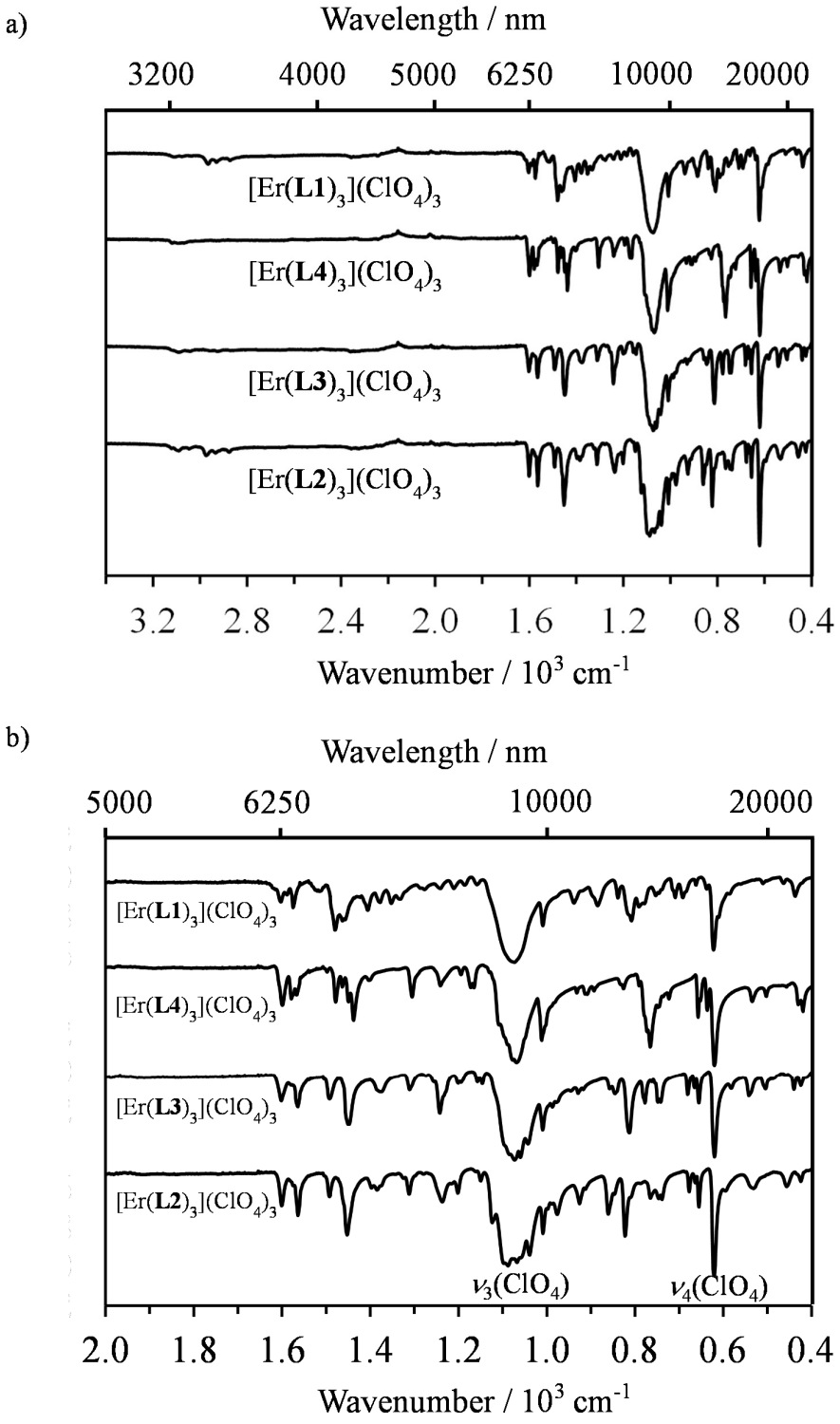

Figure S5. IR spectra of a) 1:3 complexes [Er(L***k***)3](ClO4)3 (L***k*** = **L1**-**L4**) and b) enlargement of the 400-2000 cm^{-1} fingerprint domains.

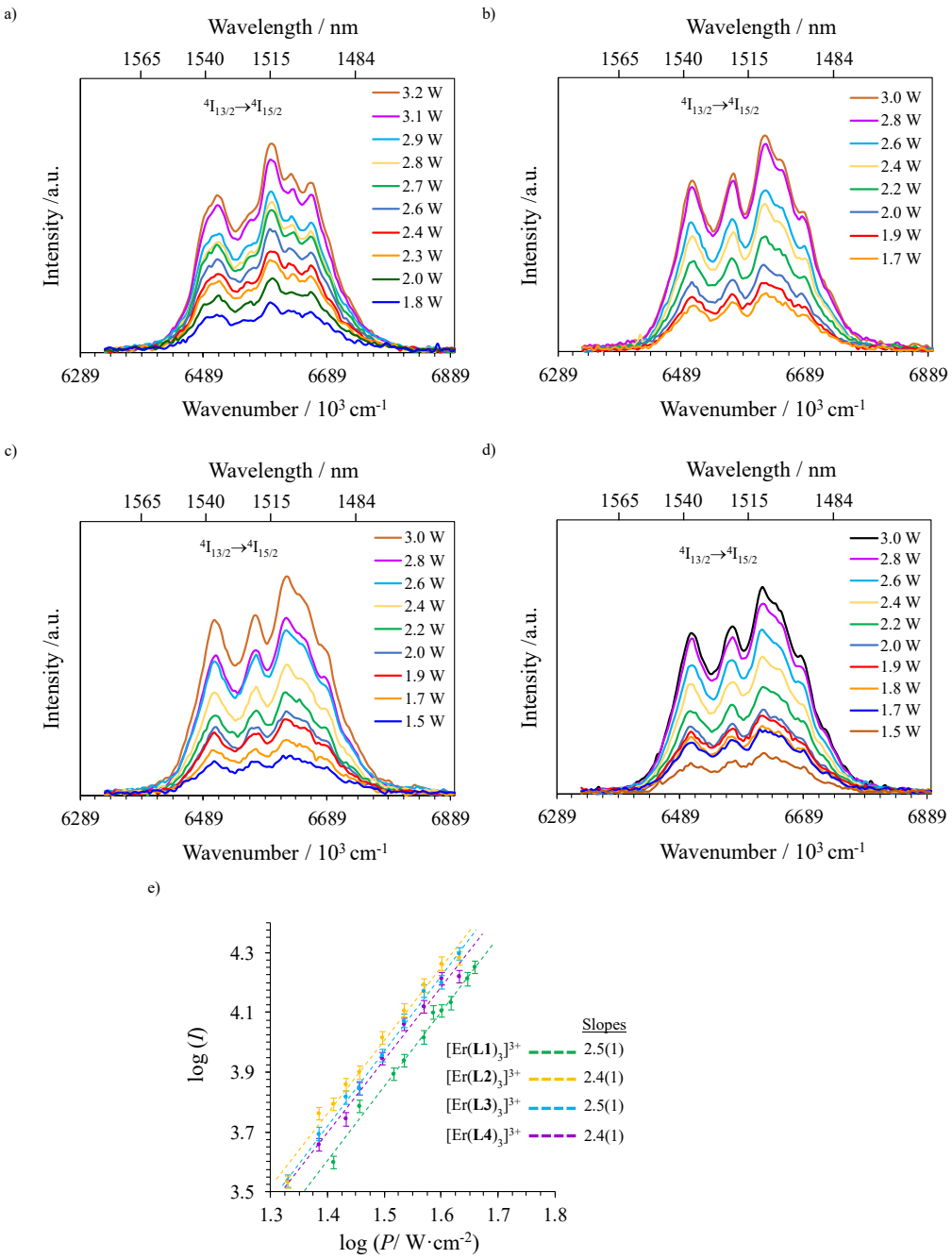

Figure S6. Near-infrared downshifted Er($^4I_{13/2}\rightarrow{}^4I_{15/2}$) emission observed for a) [Er(**L1**)$_3$](ClO$_4$)$_3$, b) [Er(**L4**)$_3$](ClO$_4$)$_3$, c) [Er(**L3**)$_3$](ClO$_4$)$_3$ and d) [Er(**L2**)$_3$](ClO$_4$)$_3$ in acetonitrile (10 mM, 298 K) upon laser excitation of the Er($^4I_{11/2}\leftarrow{}^4I_{15/2}$) transition at λ_{exc} = 966 nm ($\tilde{\nu}_{exc}$ = 10350 cm^{-1}) and for different incident pump intensities focused on a spot size of ≈ 0.07 cm^2 and e) corresponding log-log plots of downshifted intensities I as a function of incident pump intensities P (in W·cm^{-2}). The straight lines correspond to extrapolated linear fits.

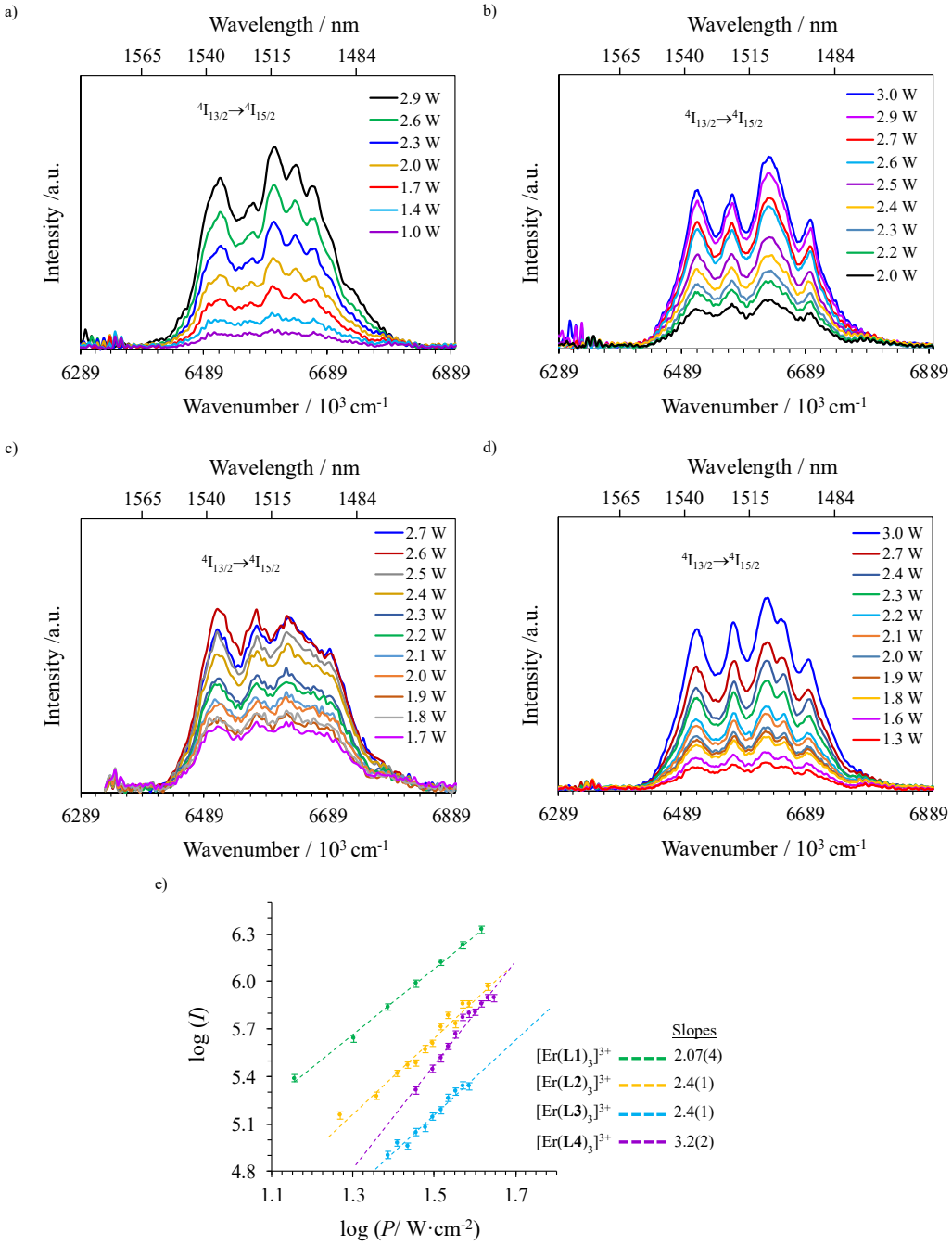

Figure S7. Near-infrared downshifted Er($^4I_{13/2}\rightarrow{}^4I_{15/2}$) emission observed for a) [Er(**L1**)$_3$](ClO$_4$)$_3$, b) [Er(**L4**)$_3$](ClO$_4$)$_3$, c) [Er(**L3**)$_3$](ClO$_4$)$_3$ and d) [Er(**L2**)$_3$](ClO$_4$)$_3$ in the solid state (298 K) upon laser excitation of the Er($^4I_{11/2}\leftarrow{}^4I_{15/2}$) transition at λ_{exc} = 966 nm ($\tilde{\nu}_{exc}$ = 10350 cm^{-1}) and for different incident pump intensities focused on a spot size of ≈ 0.07 cm^2 and e) corresponding log-log plots of downshifted intensities I as a function of incident pump intensities P (in W·cm^{-2}). The straight lines correspond to extrapolated linear fits.

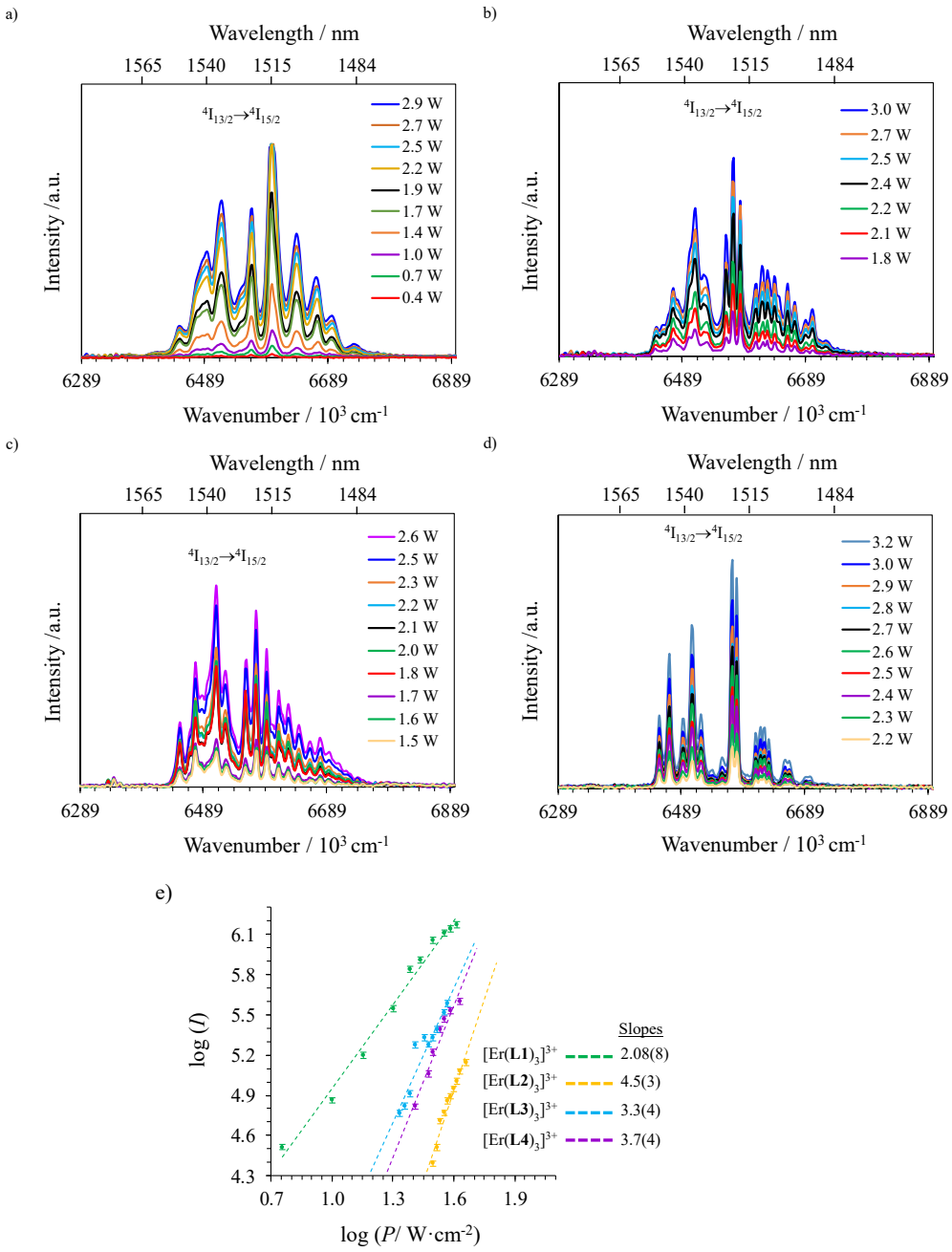

Figure S8. Near-infrared downshifted Er($^4I_{13/2}\rightarrow{}^4I_{15/2}$) emission observed for a) [Er(**L1**)$_3$](ClO$_4$)$_3$ (20 K), b) [Er(**L4**)$_3$](ClO$_4$)$_3$ (102 K), c) [Er(**L3**)$_3$](ClO$_4$)$_3$ (122 K) and d) [Er(**L2**)$_3$](ClO$_4$)$_3$ (116 K) in the solid state upon laser excitation of the Er($^4I_{11/2}\leftarrow{}^4I_{15/2}$) transition at λ_{exc} = 966 nm ($\tilde{\nu}_{exc}$ = 10350 cm^{-1}) and for different incident pump intensities focused on a spot size of ≈ 0.07 cm^2 and e) corresponding log-log plots of downshifted intensities *I* as a function of incident pump intensities *P* (in W·cm^{-2}). The straight lines correspond to extrapolated linear fits.

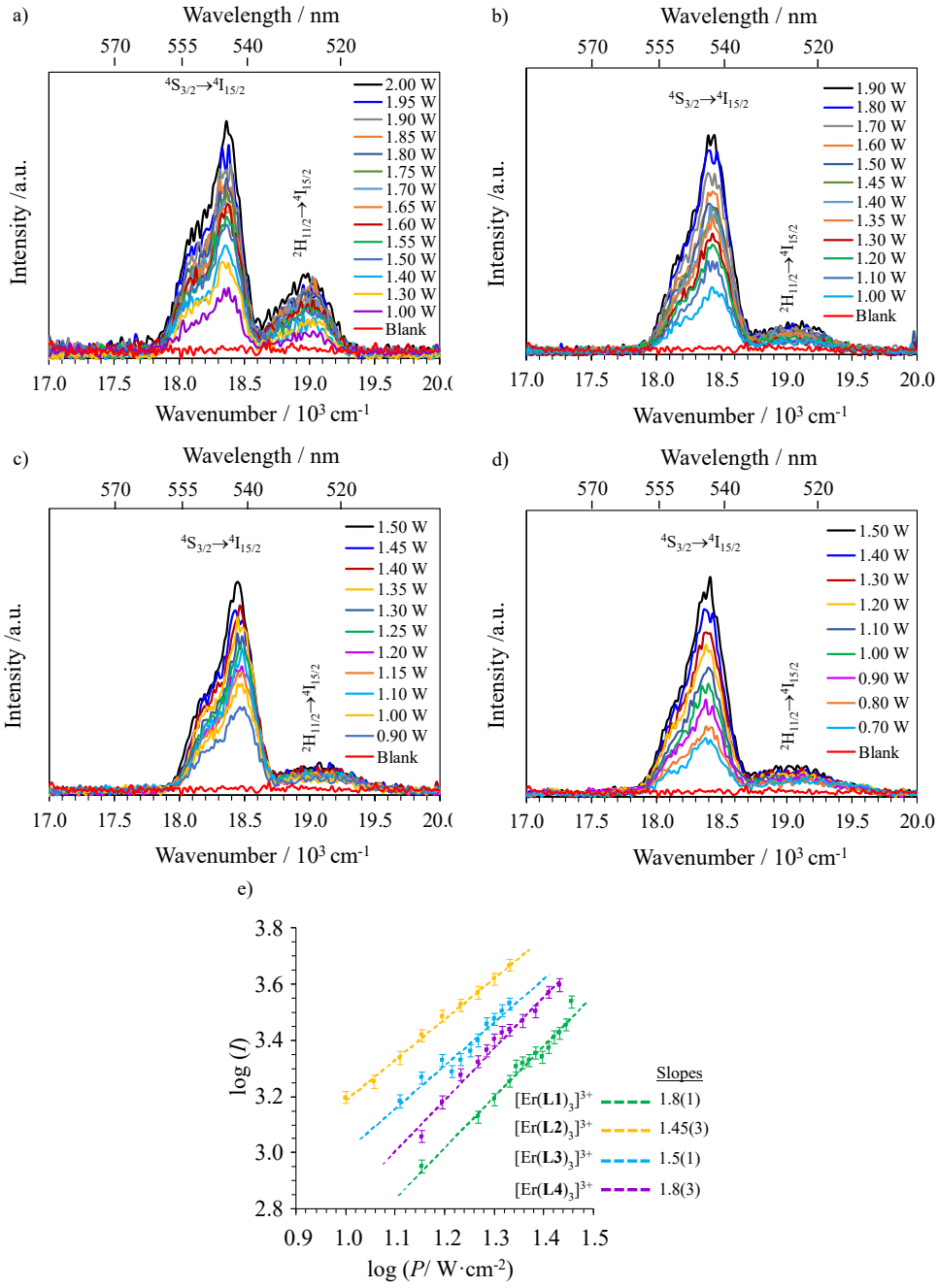

Figure S9. Upconverted visible Er($^2H_{11/2}\rightarrow{}^4I_{15/2}$) and Er($^4S_{3/2}\rightarrow{}^4I_{15/2}$) emissions observed for a) [Er(**L1**)$_3$](ClO$_4$)$_3$, b) [Er(**L4**)$_3$](ClO$_4$)$_3$, c) [Er(**L3**)$_3$](ClO$_4$)$_3$ and d) [Er(**L2**)$_3$](ClO$_4$)$_3$ (solid state, 298 K) recorded upon laser excitation of the Er($^4I_{9/2}\leftarrow{}^4I_{15/2}$) transition at λ_{exc} = 801 nm ($\tilde{\nu}_{exc}$ = 12284 cm^{-1}) and using increasing incident pump intensities focused on a spot size of ≈ 0.07 cm^2 (the blank (red curve) was recorded upon irradiation of the copper plate support covered with silver glue at maximum intensity P = 29 W·cm^{-2}) and e) corresponding log-log plots of upconverted intensities I_{up} as a function of incident pump intensities P (in W·cm^{-2}). The straight lines correspond to extrapolated linear fits.

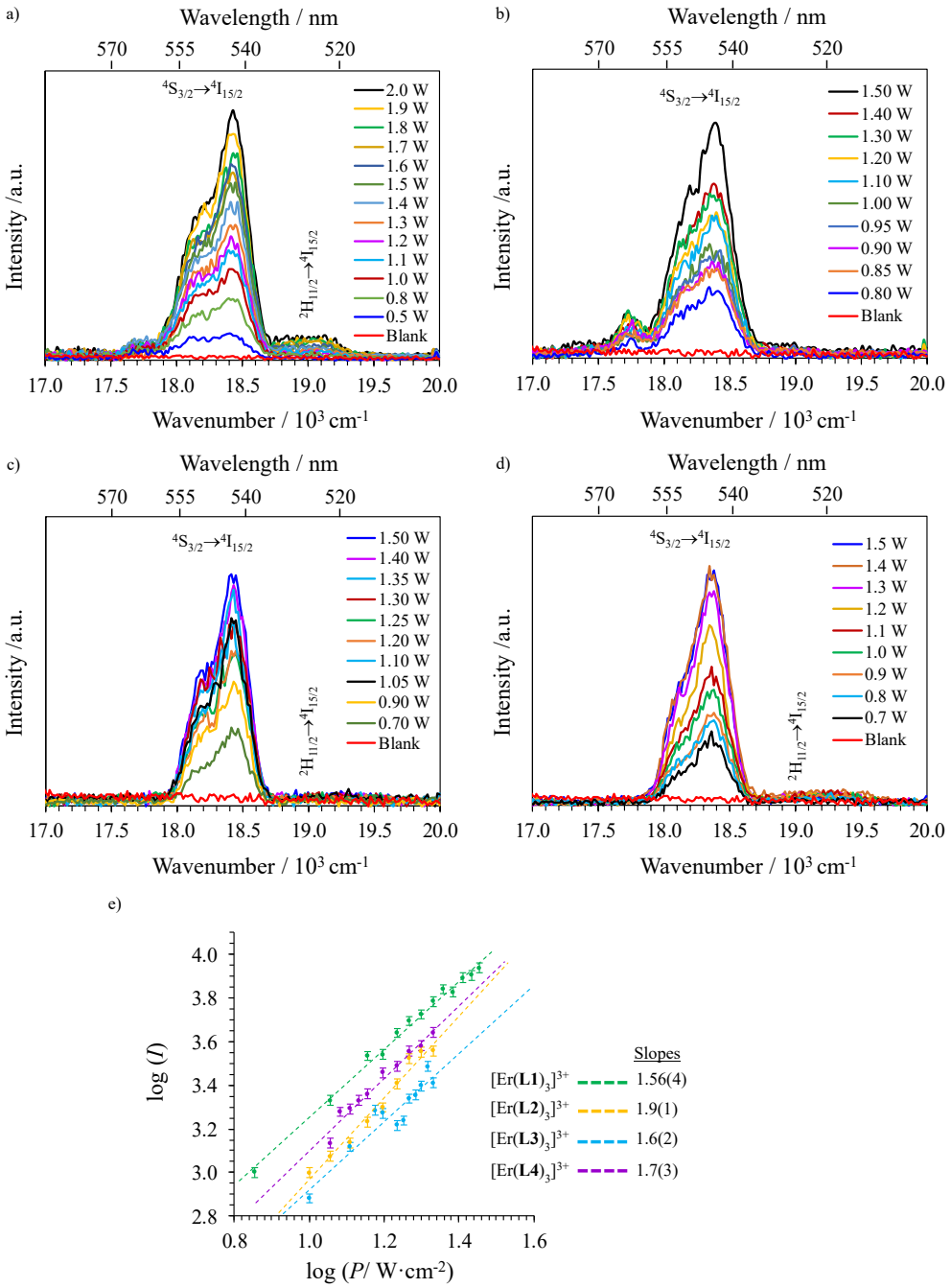

Figure S10. Upconverted visible Er($^2H_{11/2}\rightarrow{}^4I_{15/2}$) and Er($^4S_{3/2}\rightarrow{}^4I_{15/2}$) emissions observed for a) $[Er(\mathbf{L1})_3](ClO_4)_3$ (30 K), b) $[Er(\mathbf{L4})_3](ClO_4)_3$ (105 K), c) $[Er(\mathbf{L3})_3](ClO_4)_3$ (122 K) and d) $[Er(\mathbf{L2})_3](ClO_4)_3$ (113 K) recorded in the solid state upon laser excitation of the Er($^4I_{9/2}\leftarrow{}^4I_{15/2}$) transition at $\lambda_{exc} = 801$ nm ($\tilde{\nu}_{exc} = 12284$ cm^{-1}) and using increasing incident pump intensities focused on a spot size of ≈ 0.07 cm^2 (the blank (red curve) was recorded upon irradiation of the copper plate support covered with silver glue at maximum intensity $P = 29$ W·cm^{-2}) and e) corresponding log-log plots of upconverted intensities I_{up} as a function of incident pump intensities P (in W·cm^{-2}). The straight lines correspond to extrapolated linear fits.

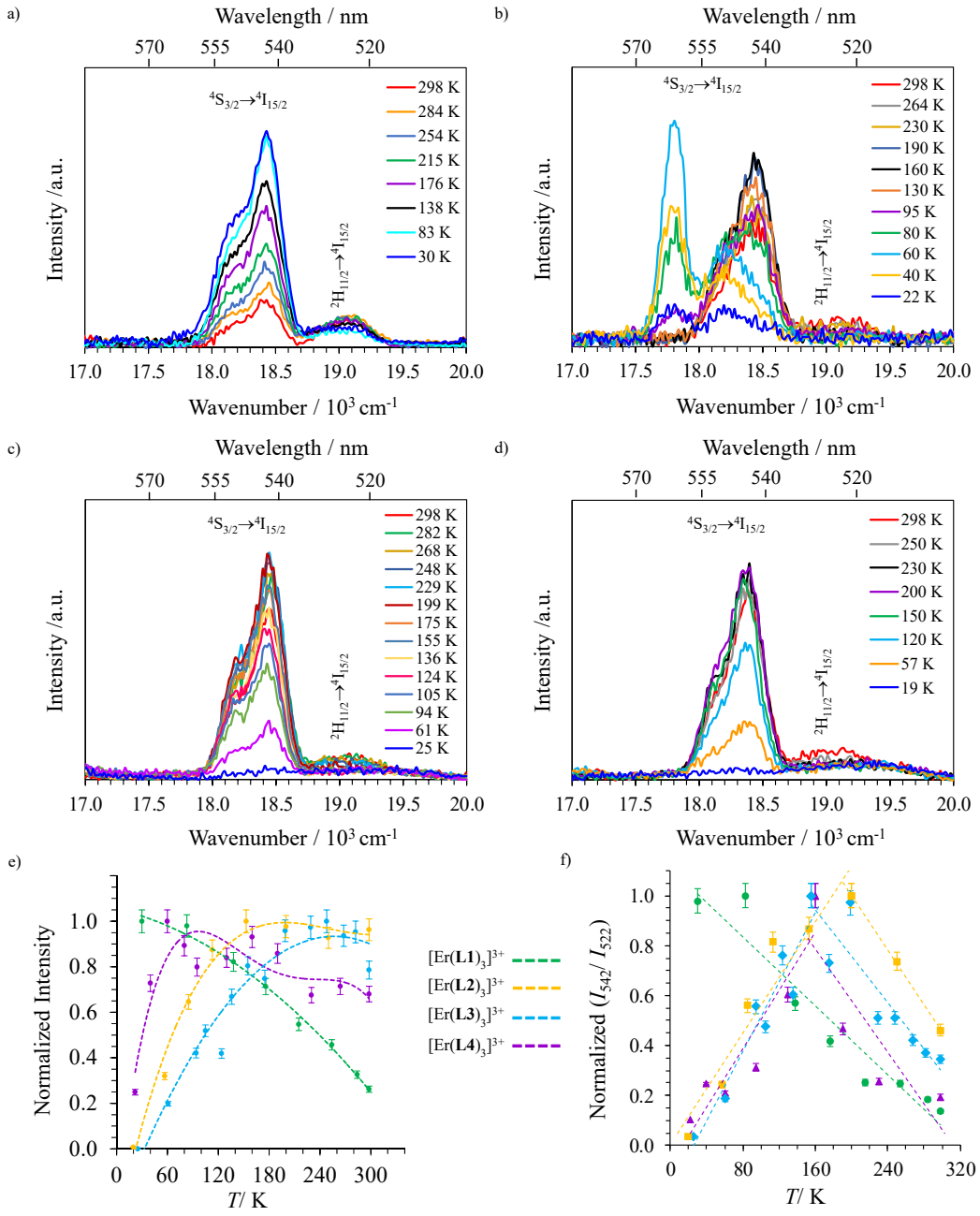

Figure S11. Upconverted visible Er($^2H_{11/2}\rightarrow{}^4I_{15/2}$) and Er($^4S_{3/2}\rightarrow{}^4I_{15/2}$) emissions observed for a) [Er(**L1**)$_3$](ClO$_4$)$_3$, b) [Er(**L4**)$_3$](ClO$_4$)$_3$, c) [Er(**L3**)$_3$](ClO$_4$)$_3$ and d) [Er(**L2**)$_3$](ClO$_4$)$_3$ (solid state, P = 29 W·cm^{-2} focused on a spot size of ≈ 0.07 cm^2) upon laser excitation of the Er($^4I_{9/2}\leftarrow{}^4I_{15/2}$) transition at λ_{exc} = 801 nm ($\tilde{\nu}_{exc}$ = 12284 cm^{-1}) and for different temperatures and e) associated dependences of the Er-centered upconverted emission intensity as a function of temperature(the dashed lines are only guides for eyes). f) Temperature dependence of the ratio of I_{542}^{up} (referred to as the intensity of Er($^4S_{3/2}\rightarrow{}^4I_{15/2}$) transition) to I_{522}^{up} (referred to as the intensity of Er($^2H_{11/2}\rightarrow{}^4I_{15/2}$) transition). The dashed lines are only guides for the eyes.

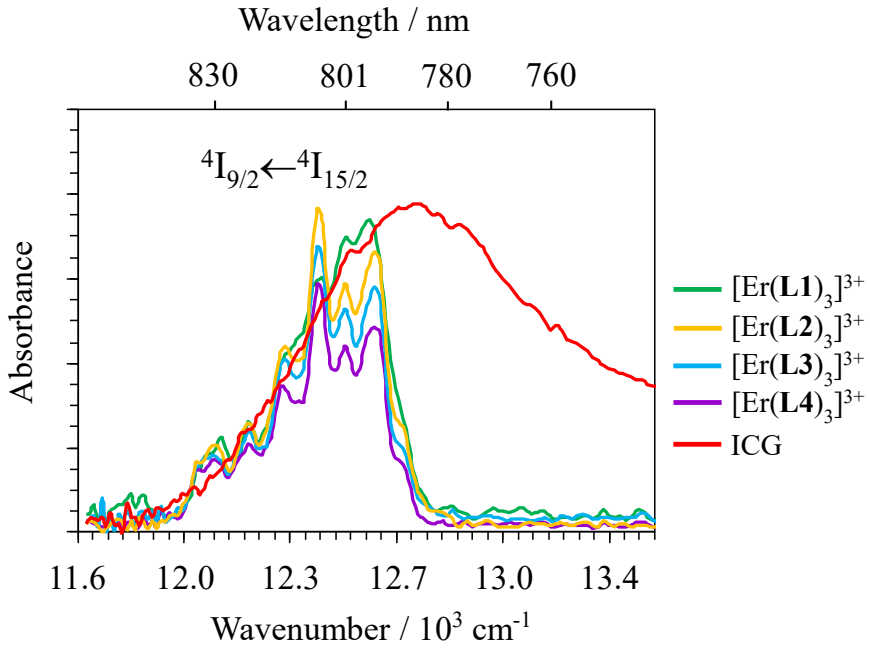

Figure S12. Absorption spectra of the mononuclear erbium complexes [Er(**L*k***)$_3$]$^{3+}$ (**L*k*** = **L1**-**L4**) in acetonitrile (c ~ 10 mM) as well as ICG (indocyanine green) in ethanol at 298 K highlighting the approximately similar optical densities at λ = 801 nm for the solutions employed for quantum yield measurements.

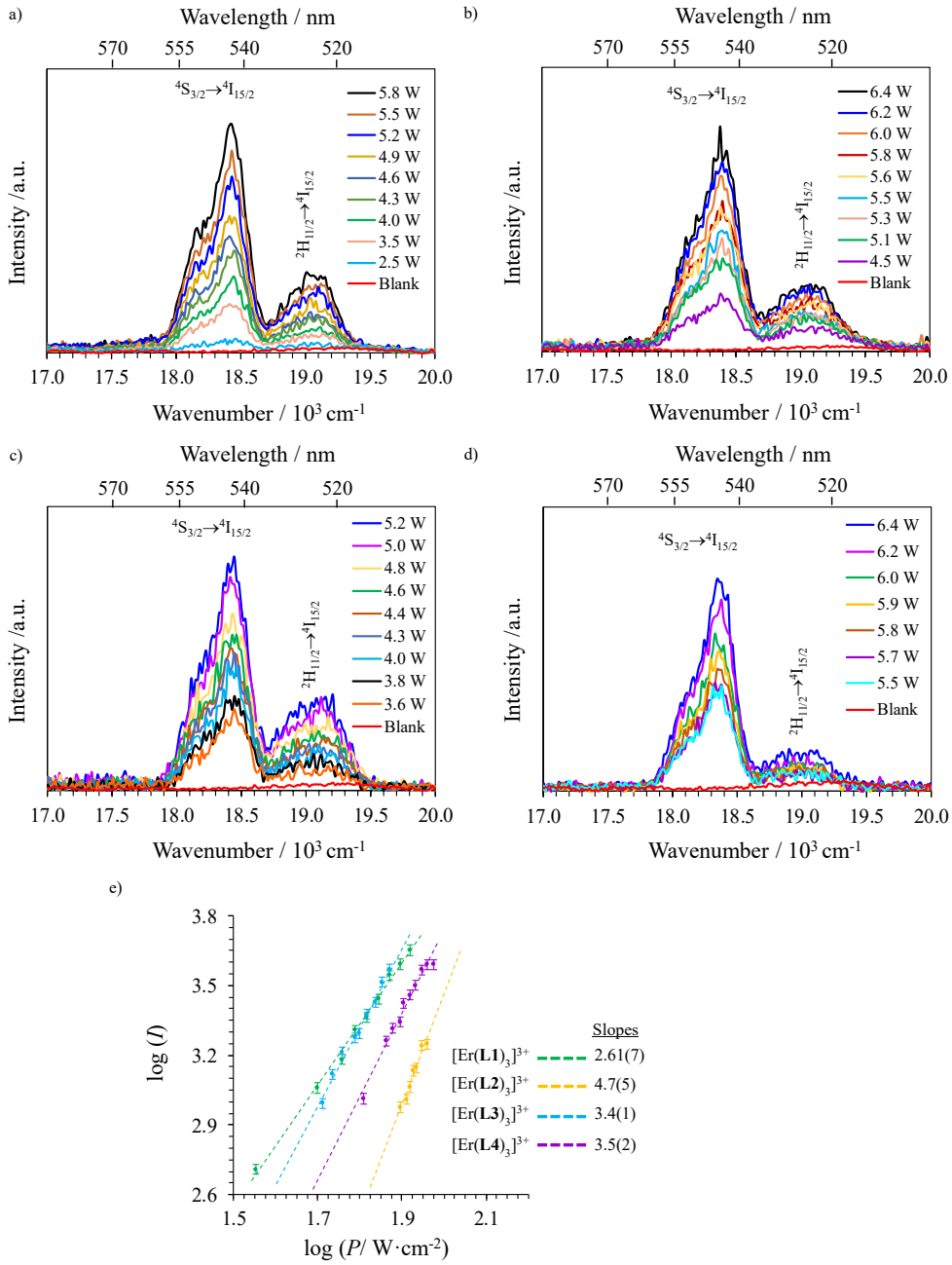

Figure S13. Upconverted visible Er($^2H_{11/2}\rightarrow{}^4I_{15/2}$) and Er($^4S_{3/2}\rightarrow{}^4I_{15/2}$) emissions observed for a) [Er(**L1**)$_3$](ClO$_4$)$_3$, b) [Er(**L4**)$_3$](ClO$_4$)$_3$, c) [Er(**L3**)$_3$](ClO$_4$)$_3$ and d) [Er(**L2**)$_3$](ClO$_4$)$_3$ (solid state, 298 K) recorded upon laser excitation of the Er($^4I_{11/2}\leftarrow{}^4I_{15/2}$) transition at λ_{exc} = 966 nm ($\tilde{\nu}_{exc}$ = 10350 cm^{-1}) and using increasing incident pump intensities focused on a spot size of ≈ 0.07 cm^2 (the blank (red curve) was recorded upon irradiation of the copper plate support covered with silver glue at maximum intensity P = 71 W·cm^{-2}) and e) corresponding log-log plots of upconverted intensities I_{up} as a function of incident pump intensities P (in W·cm^{-2}). The straight lines correspond to extrapolated linear fits.

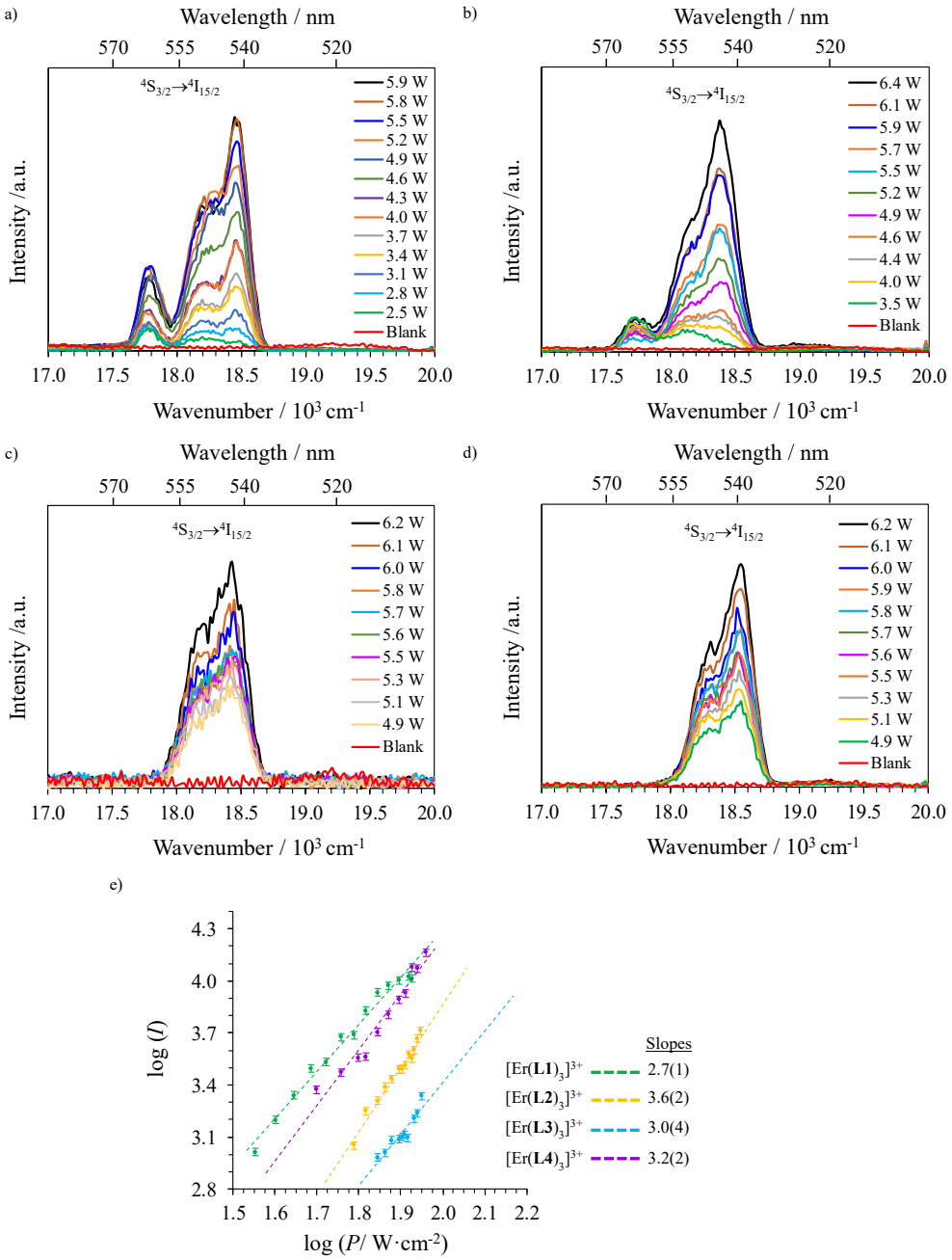

Figure S14. Upconverted visible Er($^2H_{11/2}\rightarrow{}^4I_{15/2}$) and Er($^4S_{3/2}\rightarrow{}^4I_{15/2}$) emissions observed for a) $[Er(\mathbf{L1})_3](ClO_4)_3$ (52 K), b) $[Er(\mathbf{L3})_3](ClO_4)_3$ (58 K), c) $[Er(\mathbf{L2})_3](ClO_4)_3$ (63 K) and d) $[Er(\mathbf{L4})_3](ClO_4)_3$ (58 K) recorded in the solid state upon laser excitation of the Er($^4I_{11/2}\leftarrow{}^4I_{15/2}$) transition at $\lambda_{exc} = 966$ nm ($\tilde{\nu}_{exc} = 10350$ cm^{-1}) and using increasing incident pump intensities focused on a spot size of ≈ 0.07 cm^2 (the blank (red curve) was recorded upon irradiation of the copper plate support covered with silver glue at maximum intensity $P = 71$ W·cm^{-2}) and e) corresponding log-log plots of upconverted intensities I_{up} as a function of incident pump intensities P (in W·cm^{-2}). The straight lines correspond to extrapolated linear fits,

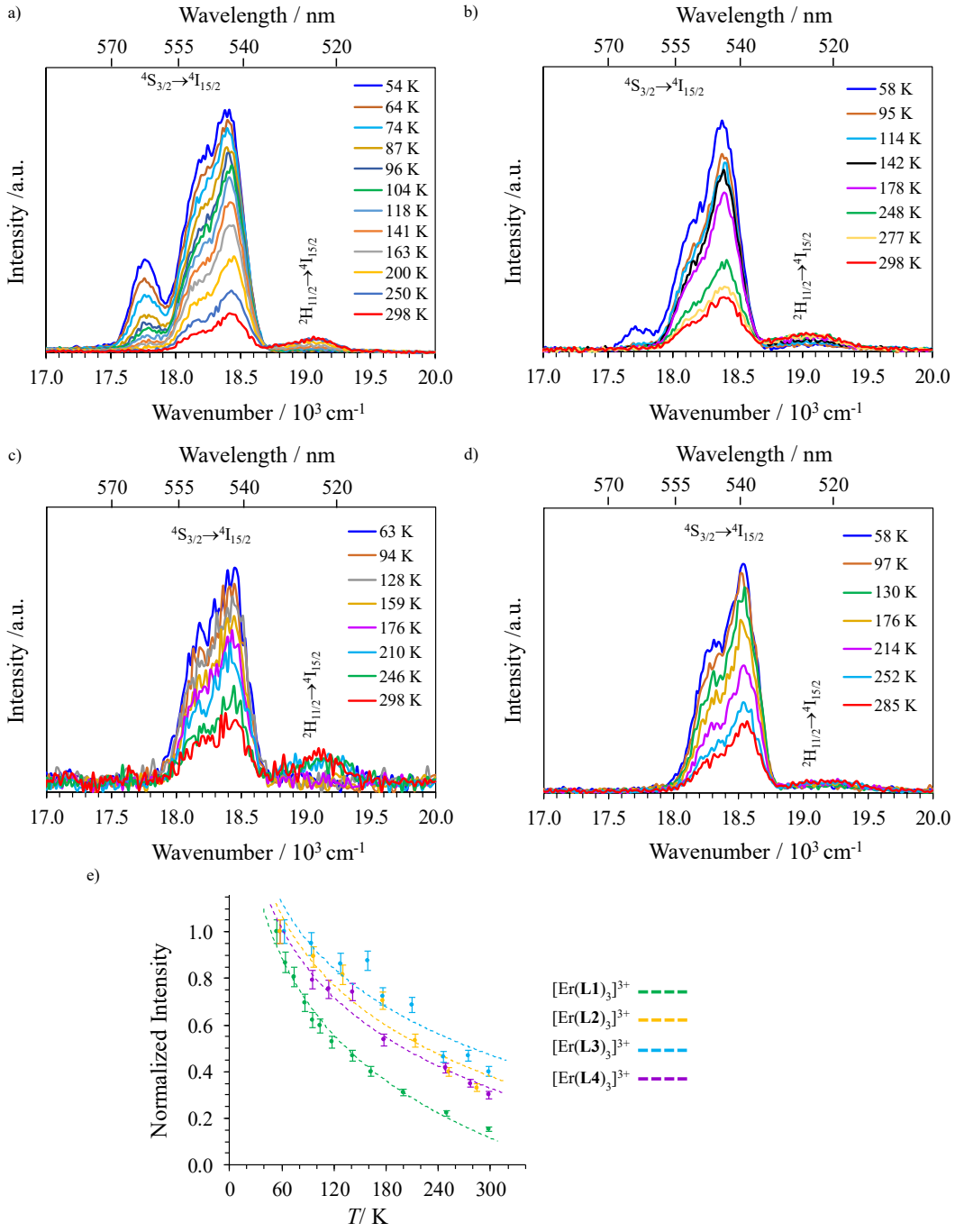

Figure S15. Upconverted visible Er($^2H_{11/2}\rightarrow{}^4I_{15/2}$) and Er($^4S_{3/2}\rightarrow{}^4I_{15/2}$) emissions observed for a) $[Er(\mathbf{L1})_3](ClO_4)_3$, b) $[Er(\mathbf{L4})_3](ClO_4)_3$, c) $[Er(\mathbf{L3})_3](ClO_4)_3$ and d) $[Er(\mathbf{L2})_3](ClO_4)_3$ (solid state, P = 64 W·cm^{-2} focused on a spot size of ≈ 0.07 cm^2) upon laser excitation of the Er($^4I_{11/2}\leftarrow{}^4I_{15/2}$) transition at λ_{exc} = 966 nm ($\tilde{\nu}_{exc}$ = 10350 cm^{-1}) and for different temperatures and e) associated dependences of the Er-centered upconverted emission intensity as a function of temperature (the dashed lines are only guides for eyes).

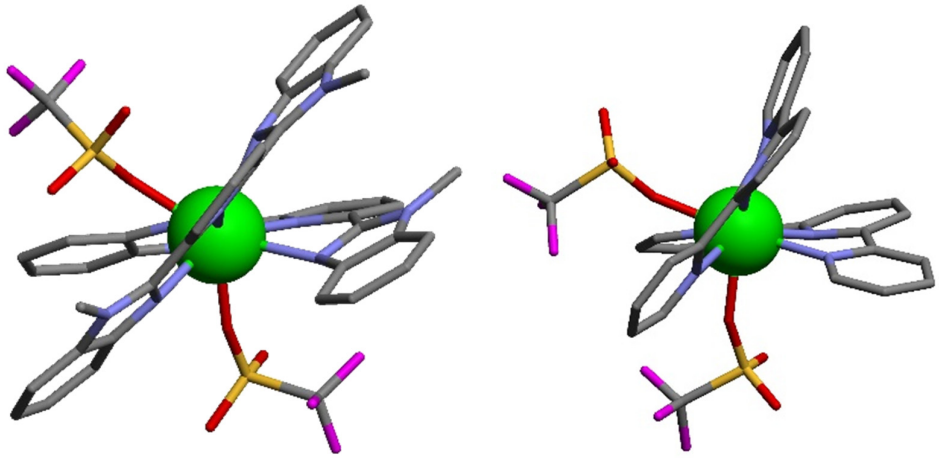

$[Er(\mathbf{L5})_2(CF_3SO_3)_2]^+$ $[Er(\mathbf{L4})_2(CF_3SO_3)_2]^+$

Figure S16. Molecular structures of mononuclear 1:2 complexes found in the crystal structures of $[Er(\mathbf{L5})_2(CF_3SO_3)_2](CF_3SO_3)\cdot 2CH_3CN$ and $[Er(\mathbf{L4})_2(CF_3SO_3)_2](CF_3SO_3)\cdot 1.5C_2H_5CN$. The counter-anions, solvent molecules and H atoms are omitted for clarity. Color code: C = grey, blue = N, red = O, yellow = S, magenta = F, green = Er.[32]